Capillary Deformations of Bendable Films

R. D. Schroll,[1,2] M. Adda-Bedia,[3] E. Cerda,[2] J. Huang,[1,4] N. Menon,[1]
T. P. Russell,[4] K. B. Toga,[4] D. Vella,[5] and B. Davidovitch[1]

[1]*Physics Department, University of Massachusetts, Amherst, Massachusetts 01003, USA*
[2]*Departamento de Física, Universidad de Santiago, Avenida Ecuador 3493, Santiago, Chile*
[3]*Laboratoire de Physique Statistique, Ecole Normale Supérieure, UPMC Paris 06, Université Paris Diderot, CNRS, 24 rue Lhomond, 75005 Paris, France*
[4]*Department of Polymer Science and Engineering, University of Massachusetts, Amherst, Massachusetts 01003, USA*
[5]*Oxford Centre for Collaborative Applied Mathematics, Mathematical Institute, 24-29 St Giles, Oxford OX1 3LB, United Kingdom*

(Received 3 February 2013; revised manuscript received 9 May 2013; published 3 July 2013)

We address the partial wetting of liquid drops on ultrathin solid sheets resting on a deformable foundation. Considering the membrane limit of sheets that can relax compression through wrinkling at negligible energetic cost, we revisit the classical theory for the contact of liquid drops on solids. Our calculations and experiments show that the liquid-solid-vapor contact angle is modified from the Young angle, even though the elastic bulk modulus (E) of the sheet is so large that the ratio between the surface tension γ and E is of molecular size. This finding indicates a new elastocapillary phenomenon that stems from the high bendability of very thin elastic sheets rather than from material softness. We also show that the size of the wrinkle pattern that emerges in the sheet is fully predictable, thus resolving a puzzle in modeling "drop-on-a-floating-sheet" experiments and enabling a quantitative, calibration-free use of this setup for the metrology of ultrathin films.

DOI: 10.1103/PhysRevLett.111.014301 PACS numbers: 46.32.+x, 46.70.De, 68.08.Bc

The partial wetting of liquids on solids is among the most basic of capillary phenomena [1]. The fundamental Young's law relates the equilibrium contact angle ϑ_Y of a liquid drop on a solid to the surface energies via

$$\cos\vartheta_Y = (\gamma_{sv} - \gamma_{s\ell})/\gamma, \tag{1}$$

where γ_{sv}, $\gamma_{s\ell}$, and $\gamma = \gamma_{\ell v}$ are the mutual surface energies between the solid, vapor, and liquid. This classical equation reflects a balance of forces on the contact line only in the plane of the solid surface and assumes that the normal component of the contact force ($\approx \gamma \sin\vartheta_Y$) induces only slight, localized deformations of the solid. However, the normal force balance must be considered when the length $\ell_m \equiv \gamma/E$ (with E the Young modulus of the solid) is larger than molecular scales [2–4]. Here, minimization of the total energy, involving interfacial and elastic components, requires a deviation of the contact angle from ϑ_Y.

A totally different notion of elastocapillarity is realized when a liquid drop is brought into contact with a stiff thin sheet of thickness t that rests on a soft, easily deformable substrate (e.g., a polystyrene sheet on water, as in Fig. 1, for which $\ell_m \approx 0.2$ Å) [5]. Here, the deformability of the foundation enables the sheet to respond to the exerted capillary force as a thin elastic body—by bending [6] and developing in-plane stresses [7]. Furthermore, in ultrathin sheets where $t \sim 10$ nm, in-plane compression relaxes completely through wrinkles whose number diverges as t decreases [8–12]. The "drop-on-a-floating-sheet" experiment (Fig. 1), which allowed a systematic study of this high bendability regime, revealed a wrinkle pattern whose size was comparable to the drop's radius R (0.5–1.5 mm) [7], indicating that the capillary force may affect in-plane stresses and shape deformation on a very large lateral length $\sim R \gg t \gg \ell_m$. An important application of this system is the measurement of thickness, surface energy, and elastic moduli of ultrathin sheets from macroscale features, namely, the extent and number of wrinkles. However, previous studies have failed to provide a quantitative, predictive link [7,13].

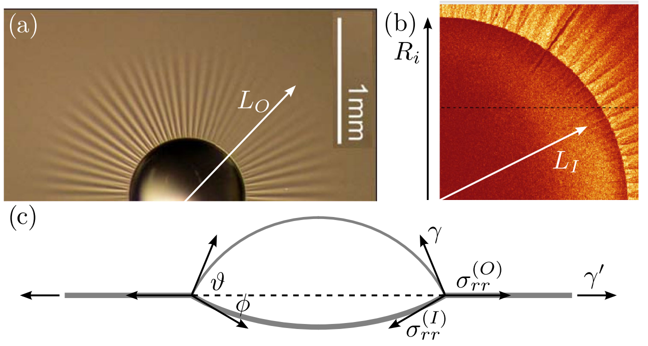

FIG. 1 (color online). (a), (b) Views of the wrinkle pattern formed by placing a water drop on a floating ultrathin polystyrene sheet ($t = 72$ nm). The radius of the contact line is R_i. Radial wrinkles appear in (a) an annular zone $R_i < r < L_O$ and (b) a narrow annulus $L_I < r < R_i$ beneath the drop. Panel (b) is obtained from confocal slices of a fluorescent sheet [14]. (c) A schematic cross section depicts the forces acting at the contact line (wrinkles are azimuthal undulations around this radial profile).

In this Letter we identify the dimensionless groups that govern elastocapillary phenomena and focus on highly bendable sheets on a highly deformable foundation. This regime is characterized by

$$\ell_m \ll t \ll \ell_m^{1/3} R^{2/3}. \tag{2}$$

Using the compression-free limit, known as the "relaxed energy" [10] or "tension field theory" [11], we show the following. (i) The contact angle between the liquid-vapor and liquid-solid interfaces [$\vartheta + \phi$ in Fig. 1(c)] deviates from ϑ_Y by an amount $\Delta\vartheta$,

$$\Delta\vartheta \sim (\ell_m/t)^{1/3}, \tag{3}$$

which vanishes slowly as $\ell_m/t \rightarrow 0$. This prediction differs from that for soft solid films on hard substrates [2,3,5], where $\Delta\vartheta$ is inversely proportional to the drop's radius. (ii) We calculate the stress profile in the sheet, from which we extract the extent of the wrinkled region and compare it with the experimental observations of [7] with no fitting of parameters. Additionally, we present data from a variant of the original experiment [7] that employs surfactants to manipulate the stress in the sheet. The agreement with our calculations substantiates the validity of our theoretical approach and its usefulness for metrology of thin solid films.

Our system is shown in Fig. 1. A circular polystyrene spin-coated sheet of radius R_O, thickness t, and Young modulus E floats on a liquid bath (whose density is ρ) and is pulled taut by the bath-vapor surface tension γ'. A small volume V of liquid of surface tension $\gamma = \gamma_{lv}$ is placed at the center of the sheet. The stretching and bending moduli of the sheet are, respectively, $Y = Et$ and $B = Et^3/12(1-\nu^2)$, where ν is the Poisson ratio. The thickness t is varied from approximately 30 to 300 nm. The radius $R_O = 23$ mm, and the Young modulus is $E = 3.4$ GPa. The distinct values of liquid surface tensions ($\gamma' \neq \gamma$) are obtained by adding surfactants to the liquid bath [14]. We define $R(V, \vartheta_Y)$ to be the radius of the contact line on an undeformed sheet: $R = (3V/2\pi)^{1/3} \times \sin\vartheta_Y(1 - 3/2\cos\vartheta_Y + 1/2\cos^3\vartheta_Y)^{-1/3}$. As Fig. 1(c) shows, the pressure in the drop forces the film to bulge, and hence the radius of the contact line, denoted here by R_i, deviates from R.

The physical parameters can be arranged into six dimensionless groups. The first two are ϑ_Y and γ/γ', which are determined by the surface energies. A second pair is

$$\tilde{K} = KR^2/\gamma', \qquad \tilde{R} = R/R_O, \tag{4}$$

where $K = \rho g$. The parameter $\tilde{K}^{-1}$ quantifies the deformability of the liquid foundation, and $\tilde{R}$ is the ratio between the sizes of the drop and the sheet. In this study we assume $\tilde{K}, \tilde{R} \rightarrow 0$, corresponding to a sufficiently small drop; the effect of $\tilde{K}, \tilde{R} \neq 0$ on the stress is perturbative [15,16]. The final pair of parameters, essential for our study, involves the elastic moduli of the sheet:

$$\tilde{\gamma} \equiv \gamma/Y = \ell_m/t, \qquad \epsilon^{-1} \equiv \gamma R^2/B \sim R^2\ell_m/t^3. \tag{5}$$

Our theory and experiments are in the regime $\tilde{\gamma}$, $\epsilon \ll 1$ [see Eq. (2)]. The parameter ϵ^{-1} is the bendability [15], and can be expressed as the ratio between the lengths R and $\sqrt{B/\gamma}$ (often called the "elastocapillary length" [6]). In the high bendability regime the sheet supports very small levels of compression before and after buckling. As a consequence, the elastic stresses in the sheet $\sigma_{rr}(r)$, $\sigma_{\theta\theta}(r)$ are determined by $\tilde{\gamma}$ (and γ/γ', ϑ_Y), and exhibit weak, subdominant dependence on the bending modulus (hence on ϵ) [15]. This feature distinguishes our system from [6], where bending forces are dominant and balance surface tension.

As Fig. 1 suggests, the two parts of the sheet separated by the contact line must be connected through boundary conditions that reflect continuity of the radial displacement field $u_r(r)$ and force balance (in $\hat{r}$) [17]:

$$u_r^{(I)} = u_r^{(O)}, \tag{6}$$

$$\sigma_{rr}^{(I)}\cos\phi + \gamma\cos\vartheta = \sigma_{rr}^{(O)}, \tag{7}$$

where $\sigma_{rr}^{(I)}$, $u_r^{(I)}$, and $\sigma_{rr}^{(O)}$, $u_r^{(O)}$, are, respectively, the radial stresses and displacements in the sheet at the inner (I) and outer (O) sides of the contact line, evaluated at $r = R_i$. The variables in Eqs. (6) and (7) are not independent. In the high bendability regime, the Föppl-von Kármán (FvK) equations that determine the displacement and stress in the sheet depend in each region on a single confinement parameter:

$$(O)\!: \tau \equiv \sigma_{rr}^{(O)}/\gamma', \qquad (I)\!: \alpha \equiv Y\gamma^2\sin^2\vartheta/2(\sigma_{rr}^{(I)})^3. \tag{8}$$

The physical meaning of α and τ will be explained below. Using the known solutions to the FvK equations [15,19], the displacements $u_r^{(I)}$, $u_r^{(O)}$ as well as the angle ϕ and the radius R_i could be eliminated from Eqs. (6) and (7), and the problem reduces to two equations for the three unknowns $\sigma_{rr}^{(I)}$, $\sigma_{rr}^{(O)}$, and ϑ. Following the proposal of [5], we find the missing relation by minimizing the total energy U_T, that consists of the elastic energy of the deformed sheet and the surface energies of the sheet, drop, and bath. The results of this calculation, whose details appear in [18], are presented in Fig. 2 for $\vartheta_Y = \pi/2$, a few distinct values of γ/γ', and a range of $\tilde{\gamma} \ll 1$.

The confinement parameters α and τ express the degree of variation of the radial tension across each part of the film, which gives rise to a compressive azimuthal (hoop) strain [15,19]. The size of the wrinkled zone thus increases with α and τ. In the outer part, τ is the ratio between the radial tension at the contact line $\sigma_{rr}^{(O)}$ and the bath tension γ'. In the inner part, α describes the ratio between the radial tensions near the center of the film and at the contact line. The latter is $\sigma_{rr}^{(I)}$ whereas the former is governed by the "geometric" stress $Y(R/\bar{R})^2$, where $\bar{R}$ is the average

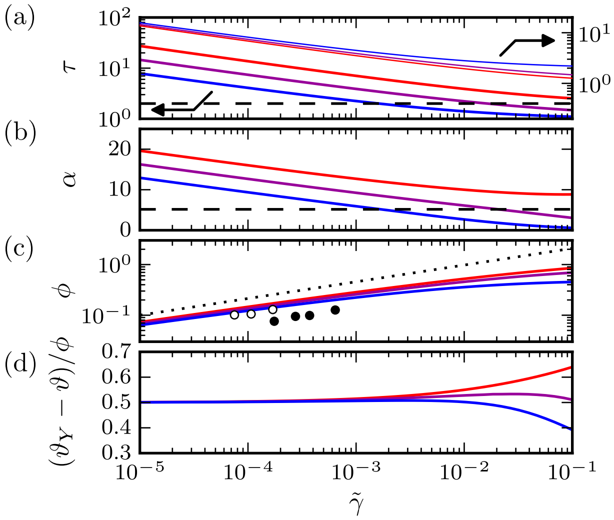

FIG. 2 (color online). (a), (b) Computed values of α, τ for $10^{-5} < \tilde{\gamma} < 10^{-1}$. Here $\vartheta_Y = \pi/2$ and γ'/γ is 2 (red line; dark gray), 1 (purple line; medium gray), 0.5 (blue line; light gray). For $\tilde{\gamma} \ll 1$ the various plots collapse upon rescaling $\tau \to \tau\gamma'/\gamma$. For sufficiently large $\tilde{\gamma}$, both α and τ are below their respective threshold values; hence, the state is unwrinkled and described by the axisymmetric solution. As $\tilde{\gamma}$ decreases, $\alpha(\tilde{\gamma})$ and $\tau(\tilde{\gamma})$ exceed their critical values (dashed lines: $\alpha_c \approx 5.16$; $\tau_c = 2$) and our calculations describe the wrinkled state of the highly bendable sheet ($\epsilon \to 0$) using the FT theory. (c) A log-log plot of the angle ϕ (see Fig. 1). Dashed line (guide to the eye) has a slope 1/3. Data points: solid circles are taken from confocal fluorescence microscopy measurements of the sheet's profile under the drop. Both bath and drop are water. The open circles are from a different, but comparable configuration (where the bath is glycerol [14]). Error bars are comparable to the symbol size. (d) The ratio $(\vartheta_Y - \vartheta)/\phi \to 1/2$ as $\tilde{\gamma} \to 0$.

radius of curvature of the bulged sheet. We estimate $\bar{R}$ from the relation $P\bar{R} \sim \sigma_{rr}^{(I)}$ that links the tension in the sheet and the Laplace pressure in the drop $P \approx \gamma/R \sin\vartheta$.

An important outcome of Refs. [15,19] is that in both inner and outer parts of the sheet the FvK equations yield two distinct solutions for the stress field, whose characteristic profiles are shown in Fig. 3. One solution, $\sigma_{rr}^{(axi)}(r)$ and $\sigma_{\theta\theta}^{(axi)}(r)$, corresponds to the axisymmetric state. Below a critical confinement ($\alpha_c \approx 5.16$ [19], $\tau_c = 2$ [20]), both radial and hoop stresses are purely tensile. However, beyond these critical values, the axisymmetric state develops hoop compression [$\sigma_{\theta\theta}^{(axi)}(r) < 0$] in annuli $L_I(\alpha) < r < R_i$ and $R_i < r < L_O(\tau)$, respectively, signaling the wrinkling instability. In the high bendability regime, $\epsilon \ll 1$, where only a tiny level of compression can be accommodated, the unstable axisymmetric stress [which is the basis for standard "near threshold" (NT) and postbuckling theories] must be replaced by a compression-free stress field that satisfies $\sigma_{\theta\theta} \geq 0$ as $\epsilon \to 0$ (see Fig. 3) [9,10]. For a given $\alpha > \alpha_c$ ($\tau > \tau_c$), the compression-free stress is the basis for a far from threshold (FT) theory of the wrinkled state [15]. The dependence of the radii L_I, L_O on the confinement demonstrates the difference between the NT and FT predictions. For the outer radius [15,20],

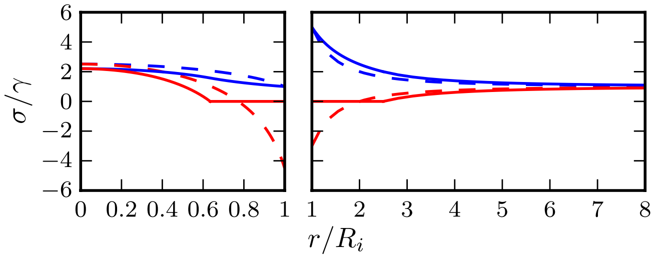

FIG. 3 (color online). The stresses σ_{rr} [light gray (blue) line] and $\sigma_{\theta\theta}$ [dark gray (red) line] beneath the drop [(I), left] and outside the contact line [(O), right] for representative post-threshold values of the confinements: $\alpha = 100$, $\tau = 5$. Solid curves are the compression-free (FT) limit [15,19]. Dashed curves are the axisymmetric (NT) limit.

$$\text{NT}: L_O = R_i\sqrt{\tau - 1}, \qquad \text{FT}: L_O = R_i\tau/2, \tag{9}$$

while for L_I the NT result is known only numerically and the FT behavior is $L_I = R_i(\alpha_c/\alpha)^{1/5}$ [19]. These estimates do not account for boundary layers between the wrinkled and unwrinkled zones. The associated correction to the wrinkle length vanishes slowly with ϵ [21].

Let us consider now the parameter regime $\tilde{\gamma} \ll 1$. Since the modulus Y is much larger than the surface tension γ, we expect the sheet to approach its undeformed state with $\vartheta \to \vartheta_Y$ and $\phi \to 0$. Furthermore, we expect (and confirm below) that the stresses at the contact line increase with Y, and hence can be approximated by the force balance at the contact line, Eq. (7): $\sigma_{rr}^{(I)} \approx \sigma_{rr}^{(O)}$. The continuity of displacement, Eq. (6), then yields after some algebra [18] the asymptotic relation $\alpha \sim \log(\tau)$. It is important to realize that the displacements $u_r^{(I)}$, $u_r^{(O)}$ at $r = R_i$ are determined by the stress in the whole sheet. Hence, the slow variation of α compared to τ reflects the global distribution of stress in the sheet, which favors hoop confinement (hence, a larger wrinkled zone) outside the contact line rather than beneath the drop. Our experiments exhibit this qualitative trend. Furthermore, the finding $\alpha \sim \log(\tau)$ suggests that the scaling behavior of the various observables can be obtained (up to logarithmic corrections) by assuming α reaches a constant value as $\tilde{\gamma} \to 0$. Equation (8) then immediately implies

$$\sigma_{rr}^{(O)} \approx \sigma_{rr}^{(I)} \sim \gamma^{2/3} Y^{1/3}. \tag{10}$$

This scaling result implies that the stresses at the contact line are not affected by the "far-field" tension γ' of the bath, but only by the nontrivial elastocapillary mechanics of the sheet beneath the drop. A direct consequence of this remarkable feature is that, for any fixed value of $\tilde{\gamma}$, the confinement $\tau \sim 1/\gamma'$ [see Eq. (8) and Fig. 2(a)]. As Eq. (9) shows, the FT theory then predicts [22]

$$L_O \sim \gamma^{2/3} Y^{1/3}/\gamma' \sim t^{1/3} \tag{11}$$

[see Figs. 4(a) and 4(b)]. This scaling law differs from the empirical one proposed in the original experiment [Eq. (3) of Ref. [7]]. Another consequence of Eq. (10), which follows from the vertical force balance at the contact line ($\gamma \sin\vartheta \approx \sigma_{rr}^{(I)} \sin\phi$), is the scaling of the angle $\phi \sim \tilde{\gamma}^{1/3}$ [Fig. 2(c)]. Assuming the angle difference $\vartheta_Y - \vartheta$ is comparable (but not equal to) ϕ, one finds the scaling of the deviation $\Delta\vartheta$ from ϑ_Y, Eq. (3). Our calculation, which minimizes the total energy U_T, shows that $\vartheta_Y - \vartheta \to \phi/2$ as $\tilde{\gamma} \to 0$ [Fig. 2(d)]. We are unaware of any intuitive argument for this angular "equipartitioning."

In Fig. 2, we have already demonstrated the agreement with experiments of our theoretical treatment for deviation from the Young angle. In the thickness range probed by our measurements, the bendability is high, $\epsilon^{-1} > 10^4$, and $7 \times 10^{-5} < \tilde{\gamma} < 10^{-3}$, a parameter regime in which the FT limit is expected to apply. In Fig. 4, we compare the measured extent of the wrinkled zone outside the drop with predictions from the FT wrinkling theory. The procedure by which the wrinkle length is determined from experimental images is described in [18]. We demonstrate good agreement between data and prediction, both in Fig. 4(a), where we hold γ/γ' fixed and vary $\tilde{\gamma}$, and in Fig. 4(b), where we vary γ' for a fixed $\tilde{\gamma}$. In Fig. 4(c) we compare the predicted profile of the sheet under the drop to the experimentally determined profile. The overall form is similar, but the amplitude is overpredicted. The numerical difference in amplitude reflects the difference between prediction and measurement in Fig. 2(c). However, as shown in that figure, the scaling of the amplitude with $\tilde{\gamma}$ is correctly recovered. The numerical difference in the amplitude also appears not to affect the successful prediction of the external wrinkle length L_O, thus enabling the use of this geometry as a quantitative probe of the mechanics of sheets.

Our work explains the wrinkle length in Fig. 1(a) [Eq. (11)], a puzzle first posed in Refs. [7,13]. We also predicted a change in the contact angle [Eq. (3)]. Beyond the regime addressed here, the four dimensionless parameters, Eqs. (4) and (5), constitute a framework for classifying elastocapillary phenomena. Their importance can be appreciated by considering previous studies [3,5,6]. To do so, we generalize the stiffness K [Eq. (4)] to account for elastic substrates of modulus E_s, setting $K \approx E_s/R$ (with R a characteristic deformation scale); this gives a deformability $\tilde{K}^{-1} \approx \gamma/RE_s$. References [3,4] addressed soft films on undeformable substrates ($\tilde{K} \gg 1$), and found that the film deforms as a 3D body in a region of size t near the contact line. Our study pertains to a stiff thin film ($\tilde{\gamma} \ll 1$) on a highly deformable foundation ($\tilde{K} \ll 1$) and exhibits different behavior: the sheet responds to capillary forces as a thin body by bending and stretching [5]. While this limit is reminiscent of [6], there $\epsilon \lesssim O(1)$ (rather than $\epsilon \ll 1$ here) and thus bending forces can balance compression; additionally, Ref. [6] studied the limit $\tilde{R} = R/R_O = O(1)$ while we have the case $\tilde{R} \ll \tilde{K}^{1/2} \ll 1$, so that a developable stress-free shape is impossible. The wildly different behavior exhibited in each of these three examples shows the importance of the four parameters in Eqs. (4) and (5) and demonstrates the rich variety of phenomena in this parameter space that remain to be explored.

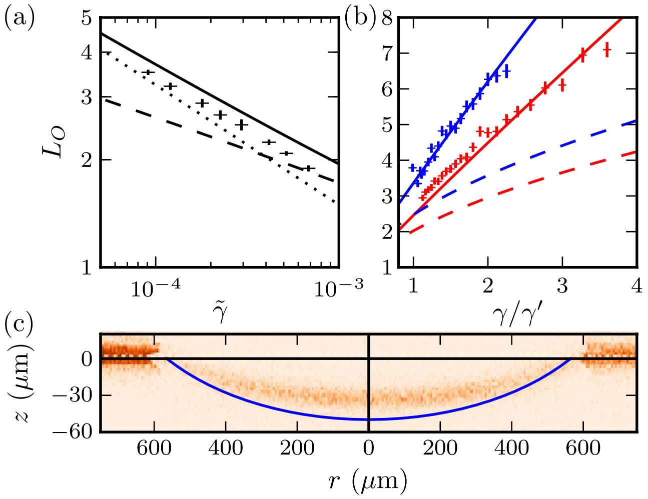

FIG. 4 (color online). (a), (b) Comparison between observed and predicted wrinkle radius L_O (normalized by R_i). Predictions shown for the FT (solid lines) and NT (dashed lines) theories. In (a), $\gamma = \gamma' = 72$ dyn/cm and $\tilde{\gamma}$ varies (data obtained by varying t from 31 to 233 nm [7]). The dotted line has a slope $-1/3$. In (b), $t = 50$ nm [dark gray (red) line], $t = 152$ nm [light gray (blue) line], and γ'/γ is varied using a concentration of surfactant (pefluorododecanoic acid) in the aqueous bath. Vertical error bars result from taking the standard deviation of several wrinkles. The measurement of the wrinkle length is described in [18]. (c) The measured profile beneath the drop, obtained by confocal microscopy [14] and the predicted profile (blue curve).

We acknowledge support by the Petroleum Research Fund of the American Chemical Society (R. D. S., B. D.), NSF-MRSEC on Polymers at UMass Amherst DMR 08-20506 (R. D. S., J. H., K. B. T., T. P. R.), Fondecyt Projects No. 3120228 (R. D. S.) and No. 1130579 (E. C.), Anillo Act 95 (E. C.), NSF DMR 09-07245 and DMR 12-0778 (N. M.), Grant No. KUK-C1-013-04 made by King Abdullah University of Science and Technology (D. V.), and NSF CAREER Grant No. DMR 11-51780 (B. D.).

---

[1] P. G. de Gennes, F. Brochard-Wyart, and D. Quere, *Capillarity and Wetting Phenomena: Drops, Bubbles, Pearls, Waves* (Springer, New York, 2003).

[2] M. E. R. Shanahan, J. Adhes. **18**, 247 (1985).

[3] R. W. Style, R. Boltyanskiy, Y. Che, J. S. Wettlaufer, L. A. Wilen, and E. R. Dufresne, Phys. Rev. Lett. **110**, 066103 (2013).

[4] R. W. Style and E. R. Dufresne, Soft Matter **8**, 7177 (2012).

[5] J. Olives, J. Phys. Condens. Matter **5**, 2081 (1993); SIAM J. Appl. Math. **56**, 480 (1996).

[6] C. Py, P. Reverdy, L. Doppler, J. Bico, B. Roman, and C. Baroud, Phys. Rev. Lett. **98**, 156103 (2007).

[7] J. Huang, M. Juszkiewicz, W. H. de Jeu, E. Cerda, T. Emrick, N. Menon, and T. P. Russell, Science **317**, 650 (2007).

[8] H. Wagner, Z. Flug. Motor. **20**, 8 (1929).

[9] M. Stein and J. M. Hedgepeth, NASA Technical Note D-813, 1961.

[10] A. C. Pipkin, IMA J. Appl. Math. **36**, 85 (1986).

[11] E. H. Mansfield, *The Bending and Stretching of Plates* (Cambridge University Press, Cambridge, England, 1989).

[12] E. Cerda and L. Mahadevan, Phys. Rev. Lett. **90**, 074302 (2003).

[13] D. Vella, M. Adda-Bedia, and E. Cerda, Soft Matter **6**, 5778 (2010).

[14] K. B. Toga, J. Huang, K. Cunningham, T. P. Russell, and N. Menon, Soft Matter (in press).

[15] B. Davidovitch, R. D. Schroll, D. Vella, M. Adda-Bedia, and E. A. Cerda, Proc. Natl. Acad. Sci. U.S.A. **108**, 18 227 (2011).

[16] J. Huang, B. Davidovitch, C. D. Santangelo, T. P. Russell, and N. Menon, Phys. Rev. Lett. **105**, 038302 (2010).

[17] In Ref. [18] we show that continuity and force balance in $\hat{\xi}$ are automatically satisfied.

[18] See Supplemental Material at http://link.aps.org/supplemental/10.1103/PhysRevLett.111.014301 for details of calculations and experimental procedures.

[19] H. King, R. D. Schroll, B. Davidovitch, and N. Menon, Proc. Natl. Acad. Sci. U.S.A. **109**, 9716 (2012).

[20] S. P. Timoshenko and J. N. Goodier, *Theory of Elasticity* (McGraw-Hill, New York, 1961).

[21] B. Davidovitch, R. D. Schroll, and E. Cerda, Phys. Rev. E **85**, 066115 (2012).

[22] The prefactor and logarithmic corrections to Eq. (11) are given in Eq. (46) of Ref. [18].